Appl Phys B (2011) 104:633–638
DOI 10.1007/s00340-011-4579-z

Applied Physics B
Lasers and Optics

Observation of polarization-controlled spatial splitting of four-wave mixing in a three-level atomic system

Z. Wang · Y. Zhang · P. Li · S. Sang · C. Yuan · H. Zheng · C. Li · M. Xiao

Received: 9 November 2010 / Revised version: 4 March 2011 / Published online: 25 May 2011

Abstract We report experimental observations of intensity modulation and spatial splitting of four-wave mixing (FWM) signal beams which can be effectively controlled by the polarization states of the pumping laser beams. Due to the periodic change of the pumping beam's polarization states, the intensity of the FWM beam also evolves periodically. The periodic spatial splitting phenomenon has been observed in both x- and y-directions. The cases with/without the dressing beams are compared. Such studies can be very useful in better understanding the formation of spatial solitons and for signal processing applications, such as spatial beam splitter, routing, and switching.

1 Introduction

Polarization states of the involved laser beams can play important roles in four-wave mixing (FWM) processes with atomic media involving multi-Zeeman sublevels [1, 2]. Several previous experimental and theoretical studies have shown that FWM processes can be effectively controlled by changing the polarization states and frequency detunings of the involved laser beams [3, 4]. Also, when the FWM processes are modulated by different polarizations of the strong coupling fields, selective transitions among polarization dark states can occur [3–5].

As two or more laser beams pass through an atomic medium, the cross-phase modulation (XPM), as well as modified self-phase modulation (SPM), can potentially affect the propagation and spatial patterns of the propagating laser beams. Laser beam self-focusing [6] and pattern formation [7] have been extensively investigated with two laser beams propagating in atomic vapors. Recently, we have observed spatial shift [8] and spatial splitting [10–12] of the FWM beams generated in multi-level atomic systems, which can be well controlled by the additional dressing laser beams via XPM. Studies of spatial shift and splitting of the laser beams can be very useful in understanding the formation and interactions of spatial solitons [11] in the Kerr nonlinear systems and signal processing applications, such as spatial beam splitter [12, 13], routing, and switching [14].

In this paper, we first investigate the modulated beam intensities and spatial splitting of the FWM signal beams induced by changing the polarization states of the pumping laser beams in the ladder-type three-level atomic system. Different dressing conditions can control the spatial splitting in the transverse (x and y) directions. Also, periodic spatial splittings of both S- and P-polarized components of the FWM beam have been observed.

2 Theoretical model and experimental scheme

In the ladder-type three-level system (with Zeeman sublevels), as shown in Figs. 1(a) and (b), five laser beams with same diameter of about 0.2 mm are applied to the atomic system with the spatial configuration given in Figs. 1(c) and (d). The pumping laser beams $\boldsymbol{E}_1(\omega_1, \mathbf{k}_1$, and Rabi frequency $G_1)$ and $\boldsymbol{E}'_1(\omega_1, \mathbf{k}'_1, G'_1)$ (with a small angle of 0.3°

Z. Wang · Y. Zhang (✉) · P. Li · S. Sang · C. Yuan · H. Zheng · C. Li
Key Laboratory for Physical Electronics and Devices of the Ministry of Education, Xi'an Jiaotong University, Xi'an 710049, China
e-mail: ypzhang@mail.xjtu.edu.cn

M. Xiao
Department of Physics, University of Arkansas, Fayetteville, AR 72701, USA
e-mail: mxiao@uark.edu

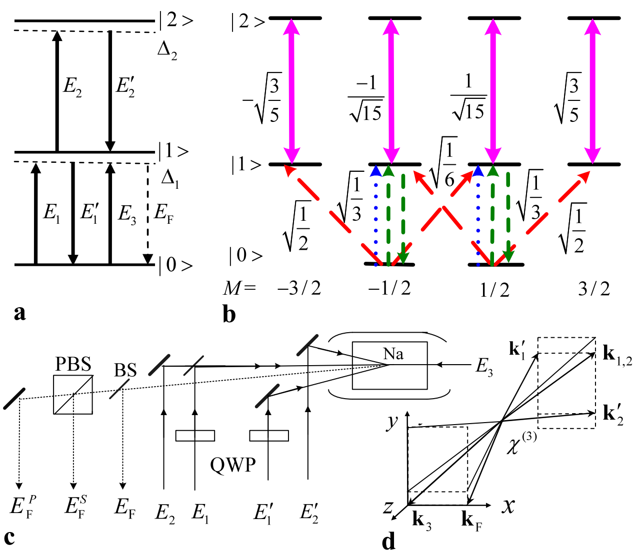

Fig. 1 (**a**) Energy level diagram to generate FWM signal $\boldsymbol{E}_\mathrm{F}$ in a ladder-type three-level atomic system. (**b**) The relevant Zeeman levels in the experiment and various transition pathways. Solid line: dressing fields G_2 and G_2'; short-dashed lines: the linearly polarized pumping fields G_1 and G_1', long-dashed lines: the circularly polarized pumping fields $G_1^{\pm}$ and $G_1'^{\pm}$; dotted line: the P-polarized probe field G_3. (**c**) The schematic diagram of the experimental configuration. (**d**) Spatial geometry for the laser beams used in the experiment

between them) are tuned to drive the transition $|0\rangle(3S_{1/2})$ to $|1\rangle(3P_{3/2})$. $\boldsymbol{E}_1$ propagates in the opposite direction of the weak probe field $\boldsymbol{E}_3(\omega_1, \mathbf{k}_3, G_3)$, as shown in Fig. 1(d). These three laser beams are from the same near-transform-limited dye laser with the same frequency detuning $\Delta_1 = \omega_{10} - \omega_1$, where ω_{10} is the transition frequency between $|0\rangle$ to $|1\rangle$, and generate an efficient degenerate FWM signal $\boldsymbol{E}_\mathrm{F}(\mathbf{k}_\mathrm{F} = \mathbf{k}_1 - \mathbf{k}_1' + \mathbf{k}_3)$ in the direction shown at the lower right corner of Fig. 1(d). Another pair of beams, $\boldsymbol{E}_2(\omega_2, \mathbf{k}_2, G_2)$ and $E_2'(\omega_2, \mathbf{k}_2', G_2')$, are the dressing beams with $\boldsymbol{E}_2$ propagating in the same direction as $\boldsymbol{E}_1$ and $\boldsymbol{E}_2'$ having a small angle (0.3°) from $\boldsymbol{E}_2$. $\boldsymbol{E}_2$ and $\boldsymbol{E}_2'$ have the same frequency detuning $\Delta_2 = \omega_{21} - \omega_2$ (from the same laser), which are tuned to the transition from $|1\rangle(3P_{3/2})$ to $|2\rangle(4D_{3/2,5/2})$. Two quarter-wave plates (QWP) are used to control the polarizations of the pumping fields $\boldsymbol{E}_1$ and $\boldsymbol{E}_1'$. The generated FWM signal is split into two parts by a 50% beam splitter (BS). One is detected directly (denoted as $\boldsymbol{E}_\mathrm{F}$), and the other decomposed into P- and S-polarized components by a polarization beam splitter (PBS), which are denoted as $\boldsymbol{E}_\mathrm{F}^\mathrm{P}$ and $\boldsymbol{E}_\mathrm{F}^\mathrm{S}$, respectively (Fig. 1(c)).

The experiment was done in Na vapor in a heat pipe at the temperature of 250°C. The atomic density is about $2.45 \times 10^{13}\ \mathrm{cm}^{-3}$. The ground state ($|0\rangle$) is the $3S_{1/2}$ energy level and the first excited state ($|1\rangle$) is the $3P_{3/2}$ level. The upper excited state ($|2\rangle$) is the $3D_{3/2}$ energy level. Both lasers (for frequencies ω_1 and ω_2) are near-transform-limited dye lasers with a repetition rate of 10 Hz and pulse width of 3.5 ns. One laser beam is split to produce beams $\boldsymbol{E}_1$, $\boldsymbol{E}_1'$, and $\boldsymbol{E}_3$ with frequency ω_1 which are tuned to the line center (589.0 nm) of the $|0\rangle$ to $|1\rangle$ transition to generate the FWM signal $\boldsymbol{E}_\mathrm{F}$. Another laser is used for beams $\boldsymbol{E}_2$ and $\boldsymbol{E}_2'$ which are tuned to the line center (568.8 nm) of the $|1\rangle$ to $|2\rangle$ transition to dress the FWM signal $\boldsymbol{E}_\mathrm{F}$. These five laser beams are carefully aligned in the spatial configuration as shown in Fig. 1(d). In order to optimize the beam shift and splitting effects, the field $\boldsymbol{E}_1'$ (energy 11 μJ) is set to be the strongest, approximately 6 times larger than $\boldsymbol{E}_1$ and $\boldsymbol{E}_2$ (energy 2 μJ), 14 times larger than the beam $\boldsymbol{E}_2'$ (energy 0.8 μJ) and 55 times larger than the weak probe beam $\boldsymbol{E}_3$ (energy 0.2 μJ), which is as weak as the generated FWM signal beam. These weak beams are recorded by a CCD.

To understand the observed changes in beam intensities and splittings of the FWM beams, we need to consider the polarization states of the beams and various SPM and XPM processes. The spatial beam breaking is mainly due to the overlap between the weak FWM beam and the strong dressing or pumping beams [6–9]. The propagation equations for the S and P polarizations of the generated FWM beam are

$$\begin{aligned}
&\frac{\partial \boldsymbol{E}_\mathrm{F}^\mathrm{P}}{\partial z} - \frac{i\nabla_\perp^2 \boldsymbol{E}_\mathrm{F}^\mathrm{P}}{2\mathbf{k}_\mathrm{F}} \\
&\quad = \frac{i\mathbf{k}_\mathrm{F}}{n_0}\Big[n_2^{\mathrm{P1}}\big|\boldsymbol{E}_\mathrm{F}^\mathrm{P}\big|^2 + 2n_2^{\mathrm{P2}}\big|\boldsymbol{E}_1'\big|^2 + 2n_2^{\mathrm{P3}}\big|\boldsymbol{E}_2'\big|^2 \\
&\qquad + 2n_2^{\mathrm{P4}}|\boldsymbol{E}_1|^2 + 2n_2^{\mathrm{P5}}|\boldsymbol{E}_2|^2\Big]\boldsymbol{E}_\mathrm{F}^\mathrm{P},
\end{aligned} \tag{1a}$$

$$\begin{aligned}
&\frac{\partial \boldsymbol{E}_\mathrm{F}^\mathrm{S}}{\partial z} - \frac{i\nabla_\perp^2 \boldsymbol{E}_\mathrm{F}^\mathrm{S}}{2\mathbf{k}_\mathrm{F}} \\
&\quad = \frac{i\mathbf{k}_\mathrm{F}}{n_0}\Big[n_2^{S1}\big|\boldsymbol{E}_\mathrm{F}^\mathrm{S}\big|^2 + 2n_2^{\mathrm{S2}}\big|\boldsymbol{E}_1'\big|^2 \\
&\qquad + 2n_2^{\mathrm{S3}}\big|\boldsymbol{E}_2'\big|^2 + 2n_2^{\mathrm{S4}}|\boldsymbol{E}_1|^2 + 2n_2^{\mathrm{S5}}|\boldsymbol{E}_2|^2\Big]\boldsymbol{E}_\mathrm{F}^\mathrm{S},
\end{aligned} \tag{1b}$$

where z is the propagation distance; $\mathbf{k}_\mathrm{F} = \omega_1 n_0/c$ is the wave vector of the FWM beam; n_0 is the linear refractive index at ω_1; $n_2^{\mathrm{P1,S1}}$ are the self-Kerr coefficients for the S and P components of $\boldsymbol{E}_\mathrm{F}$ and $n_2^{\mathrm{P2-5,S2-5}}$ are the P- and S-polarized cross-Kerr coefficients of $\boldsymbol{E}_\mathrm{F}$ induced by $\boldsymbol{E}_{1,2}'$ and $\boldsymbol{E}_{1,2}$, respectively. The Kerr coefficients can be defined as $n_2 = C\mathrm{Re}\chi^{(3)}$, where $C = (\varepsilon_0 c n_0)^{-1}$ and the Kerr nonlinear susceptibility is expressed as $\chi^{(3)} = D\rho_{10}^{(3)}$, where $D = N\mu_{10}^4/(\hbar^3\varepsilon_0 G_1|G_1|^2)$ for $n_2^{\mathrm{P1,S1}}$ and $D = N\mu_{10}^4/(\hbar^3\varepsilon_0 G_1|G_3|^2)$ for $n_2^{\mathrm{P2-5,S2-5}}$ [12]. N is the atomic density of the medium (determined by the cell temperature) and μ_{10} (μ_{20}) is the dipole matrix element between energy levels $|0\rangle$ and $|1\rangle(|2\rangle)$.

Different pumping field polarizations can generate FWM signals with different polarizations. The S-polarized component of $\boldsymbol{E}_1$ or $\boldsymbol{E}_1'$ can be decomposed into balanced left- and right-circularly polarized parts, while the P component keeps to be linearly polarized. Such polarization configuration results in S- and P-polarized FWM beams generated from different transition pathways among various Zeeman sublevels, as shown in Fig. 1(b). With different dipole moments for the transitions between $|0\rangle - |1\rangle$ and $|1\rangle - |2\rangle$, the S- and P-polarized FWM components have different appearances in both intensity modulations and spatial patterns due to nonlinear Kerr effects.

One can obtain the expression for the P-polarized FWM ($\boldsymbol{E}_{\rm F}^{\rm P}$) intensity when changing the polarization of $\boldsymbol{E}_1$: $I^{\rm P} \propto I(\sin^4\theta + \cos^4\theta)$. When changing the polarizations of both the $\boldsymbol{E}_1$ and $\boldsymbol{E}_1'$ beams, the P-polarized FWM intensity is given by $I^{\rm P} \propto I(\sin^4\theta + \cos^4\theta)[\sin^4(\theta+\theta_0) + \cos^4(\theta+\theta_0)]$ [12]. θ is the polarization angles of $\boldsymbol{E}_1$ or $\boldsymbol{E}_1'$ controlled by QWP. θ_0 is the polarization angle difference between $\boldsymbol{E}_1$ and $\boldsymbol{E}_1'$ fields. Also, one can solve the coupled density-matrix equations to obtain $\rho_{10}^{(3)}$ for $n_2^{\rm P}$ induced by the $\boldsymbol{E}_1$ and $\boldsymbol{E}_1'$ fields: $n_2^{\rm P} \propto n_2^a(\sin^4\theta + \cos^4\theta)$ [12], where $n_2^a \propto \mathrm{Re}(-iG_{\rm F}^{\rm P}F_a^{\rm P})$. Similarly, the expression of the S-polarized FWM ($\boldsymbol{E}_{\rm F}^{\rm S}$) intensity, when changing the $\boldsymbol{E}_1$ polarization, is $I^{\rm S} \propto I\sin^2\theta\cos^2\theta$. When changing polarizations of both $\boldsymbol{E}_1$ and $\boldsymbol{E}_1'$ beams, it becomes $I^{\rm S} \propto I(\sin^4\theta + \cos^4\theta)\sin^2(\theta+\theta_0)\cos^2(\theta+\theta_0)$, where $I \propto (\rho_{10}^{(3)})^2 = (-iG_3F_a^{\rm S,P})^2$. $n_2^{\rm S}$, induced by the $\boldsymbol{E}_1$ and $\boldsymbol{E}_1'$ fields, is given by $n_2^{\rm S} \propto n_2^b\sin^2\theta\cos^2\theta$, where $n_2^b \propto \mathrm{Re}(-iG_{\rm F}^{\rm S}F_a^{\rm S})$. The coefficients are $F_a^{\rm S} = (G_1^{\pm})^2/F_1^2F_2$, $F_a^{\rm S} = (G_1^{\pm} + G_1'^{\pm})^2/F_1^2F_2$ ($F_a^{\rm P} = G_1^2/F_1^2F_2$, $F_a^{\rm P} = (G_1 + G_1')^2/F_1^2F_2$) for $\boldsymbol{E}_{\rm F}^{\rm S}$($\boldsymbol{E}_{\rm F}^{\rm P}$) beam due to the $\boldsymbol{E}_1$ and $\boldsymbol{E}_1\&\boldsymbol{E}_1'$ dressings, respectively. Here, F_i $(i = 1, 2)$ is the function of the detunings and relaxation rates for different perturbation chains.

If we neglect the diffraction terms, the SPM and the small XPM contributions, and assume that all the beams involved are initially Gaussian with different centers, amplitudes and half-widths, (1a) and (1b) can be readily solved to obtain the XPM-induced phase shift $\phi = 2\mathbf{k}_{\rm F}n_2zI_1e^{-r^2/2}/(n_0I_0)$ imposed on the FWM beams by the pump fields [6]. The additional transverse propagation wave vector is $\delta\mathbf{k}_r = (\partial\phi/\partial r)\hat{r}$ and its direction is always toward the beam center of the strong pump field with positive n_2. Therefore, the weak $\boldsymbol{E}_{\rm F}$ field is shifted to the pump field center and split globally. The locally focusing and defocussing due to the spatially varied phase-front curvature $\partial^2\phi/\partial r^2$ in the $\boldsymbol{E}_{\rm F}$ beam further leads to its local splitting. The expression of the nonlinear phase shift shows that the strong spatial splitting can occur with increased I_1, n_2 and decreased I_0, here I_1 is the dressing field intensity and I_0 is the intensity of the FWM beam. In those expressions, $r = x/w_0$ and y/w_0 are the transverse coordinates, respectively, and $\hat{r}$ is the unit vector along the transverse axes. w_0 is the spot size of the FWM beam.

3 Polarization-controlled spatial splitting of the FWM beam

In the first experiment, we only turn on $\boldsymbol{E}_1, \boldsymbol{E}_1'$, and $\boldsymbol{E}_3$ beams. The FWM signal $\boldsymbol{E}_{\rm F}$ can be obtained without $\boldsymbol{E}_2$ and $\boldsymbol{E}_2'$ dressing. A QWP is used with a rotation angle θ to change the polarization state of the $\boldsymbol{E}_1$ field, we can obtain the splitting of the $\boldsymbol{E}_{\rm F}^{\rm S}$ beam for the S-polarized FWM beam (Fig. 2). Such a beam splitting formed in the atomic medium is obtained with flexible and easy to control parameters, such as atomic density, intensities of the dressing and FWM beams, and nonlinear dispersion [12]. Figure 2 presents the experimentally recorded splitting spots and the y cross-section intensity curves of the $\boldsymbol{E}_{\rm F}^{\rm S}$ beam at different polarization states of $\boldsymbol{E}_1$(with $\theta = 0°, 22.5°, 45°, 67.5°$ and $90°$, respectively) in the x-direction and different frequency detunings (with $\Delta_1 = -60.2$ GHz, -55.1 GHz, -50.7 GHz, -46.4 GHz, respectively) in the y-direction. The inverted triangle dots show that the periodic intensity change of the $\boldsymbol{E}_{\rm F}$ beam is decided by the polarization of $\boldsymbol{E}_1$ (at $\Delta_1 = -46.4$ GHz). Under this condition, $\boldsymbol{E}_1$ is strongest at $0°$ and $90°$ while weakest at $45°$. At $45°$, the nonlinear phase shift ϕ reaches its maximum value with the largest I_1/I_0 (having the constant $I_1 \propto (\boldsymbol{E}_1')^2$ and smallest $I_0 \propto (\boldsymbol{E}_{\rm F}^{\rm S})^2$), leading to the strongest splitting in the y-direction caused by $\boldsymbol{E}_1'$, of which we use the splitting number to measure. Correspondingly, the weakest y-direction splitting appears at the $0°$ and $90°$ polarization states, as shown by the y-direction splitting (circle dots) of $\boldsymbol{E}_{\rm F}^{\rm S}$ in Fig. 2. With different frequency detunings, this phenomenon changes gradually. In the self-focusing medium and near the resonance frequency, ϕ reaches its maximum, so $\boldsymbol{E}_{\rm F}^{\rm S}$ splits into more parts with corresponding polarization states of $\boldsymbol{E}_1$.

Next, in the same beam configuration (without $\boldsymbol{E}_2$ and $\boldsymbol{E}_2'$ dressing beams), we change the polarization states of both $\boldsymbol{E}_1$ and $\boldsymbol{E}_1'$ beams ($\boldsymbol{E}_1'$ is set at 45° polarization angle before $\boldsymbol{E}_1$). Figure 3 shows the experimentally measured spots, which split strongly in the y-direction at $-45°, 0°, 45°, 90°$, and weakly at $-22.5°, 22.5°$, and $67.5°$ for both the S-polarized and P-polarized FWM beams (Figs. 3(a) and (e)). The splitting in the y-direction changes with a 45° period (Figs. 3(b) and (f)). However, there only exists splitting in the x-direction for the S-polarized FWM beam (Figs. 3(a) and (c)). Moreover, the intensities of the $\boldsymbol{E}_{\rm F}^{\rm S}$ and $\boldsymbol{E}_{\rm F}^{\rm P}$ beams are shown in Figs. 3(d) and (g), respectively, which change with a $45°$ period as the polarization states of the $\boldsymbol{E}_1'$ and $\boldsymbol{E}_1$ beams are changing. These results match reasonably well with the theoretical calculations (using the split-step Fourier method) based on the coupled propagation equations (1a) and (1b) for the S- and P-polarized FWM components.

Let's first consider the behavior of $\boldsymbol{E}_{\rm F}^{\rm S}$, as shown in Figs. 3(a–d). It is interesting to note that when $\theta = \pm 45°, 0°$

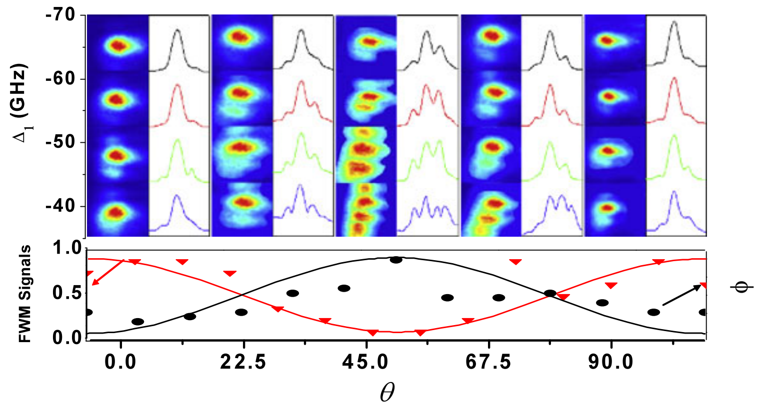

Fig. 2 The experimentally measured spots and the y cross-section intensity curves of $\boldsymbol{E}_{\mathrm{F}}^{\mathrm{S}}$ beam versus different polarization states of $\boldsymbol{E}_1$ with different frequency detunings from up to down ($G_1 = 15$ GHz and $G_1' = 20$ GHz). The curves below are the y-direction splitting number of $\boldsymbol{E}_{\mathrm{F}}^{\mathrm{S}}$ (circle dots) and the fitted ϕ solid curve, also the normalized intensity values (inverted triangle) and the corresponding theoretical solid curve versus different polarization states, with $\Delta_1 = -46.4$ GHz

and 90°, the beam splitting in the y-direction is strong, while the splitting becomes stronger in the x-direction and weaker in y-direction when $\theta = \pm 22.5°$ or 67.5° in Fig. 3(a), though the splittings in both directions have the same 45° period. This phenomenon can be explained by the relative positions between the weak FWM beams and the strong dressing beams shown in Fig. 1(b). When the polarizations of both $\boldsymbol{E}_1$ and $\boldsymbol{E}_1'$ beams ($\boldsymbol{E}_1'$ is set at 45° before $\boldsymbol{E}_1$) are changed, the intensities of $\boldsymbol{E}_1$ and $\boldsymbol{E}_1'$ alternatively reach their maximum values in the period of 90° (the $\boldsymbol{E}_1$ beam is strongest at −45° and 45°, while $\boldsymbol{E}_1'$ is strongest at 0° and 90°). First, at the 0° (or 90°) polarization state of $\boldsymbol{E}_1$, with little dressing by the weakest $\boldsymbol{E}_1$, the $\boldsymbol{E}_{\mathrm{F}}$ beam overlaps on the strongest $\boldsymbol{E}_1'$ beam in the y-direction at a special alignment, where ϕ reaches its maximum caused by $I_1 \propto (\boldsymbol{E}_1')^2$, leading to the strongest y-direction splitting (Fig. 3(a)). From $\theta = 0^{\circ}$ to $\pm 45°$, as $\boldsymbol{E}_1'$ decreasing and $\boldsymbol{E}_1$ increasing, the $\boldsymbol{E}_{\mathrm{F}}$ beam is shifted to the left direction and gets closer to $\boldsymbol{E}_1$ due to the attraction ($n_2 > 0$) of the strong $\boldsymbol{E}_1$ beam and the probe beam $\boldsymbol{E}_3$ (Fig. 1(d)). Second, at $\theta = \pm 22.5°$, $\boldsymbol{E}_{\mathrm{F}}$ partially overlaps with $\boldsymbol{E}_1$ and $\boldsymbol{E}_1'$, causing beam splitting in the x-direction (Fig. 3(a)). Third, when $\boldsymbol{E}_1$ reaches its maximum, the y-direction overlaps with the strongest $\boldsymbol{E}_1$ at $\theta = \pm 45°$ (here $I_1 \propto (\boldsymbol{E}_1)^2$), with little dressing from the weakest $\boldsymbol{E}_1'$, producing strong y-direction splitting. Thus, as the polarization states periodically change, the $\boldsymbol{E}_{\mathrm{F}}$ beam shifts back and forth between $\boldsymbol{E}_1$ and $\boldsymbol{E}_1'$ beams, so a similar phenomenon periodically appears.

Figures 3(e–g) present the experimentally measured spots, the periodic splitting in the y-direction, and the beam intensity of $\boldsymbol{E}_{\mathrm{F}}^{\mathrm{P}}$. Figures 3(f) and 3(g) are similar to Figs. 3(b) and 3(d), respectively. However, the differences between $\boldsymbol{E}_{\mathrm{F}}^{\mathrm{S}}$ and $\boldsymbol{E}_{\mathrm{F}}^{\mathrm{P}}$ can also be observed, which mainly appear on the x-direction splitting ($\theta = \pm 22.5°$ or 67.5°) and the beam intensity (0° or 90°). Here, the dipole moments of the transitions between $|0\rangle - |1\rangle$ of the S-polarized laser beams are different from that of the

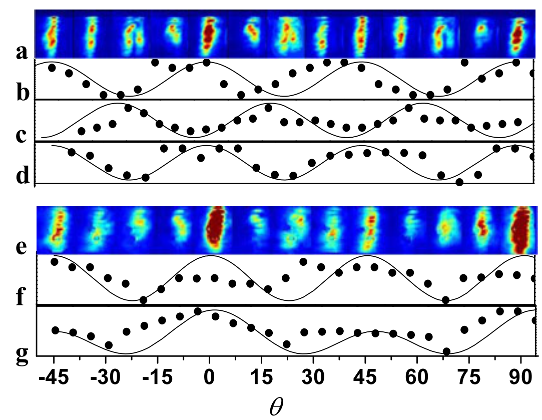

Fig. 3 The FWM beam spots (**a**, **e**), the splitting numbers in the beam's x (**c**) and y (**b**, **f**) directions, the intensities (**d**, **g**) of the $\boldsymbol{E}_{\mathrm{F}}^{\mathrm{S}}$ (**a–d**) and $\boldsymbol{E}_{\mathrm{F}}^{\mathrm{P}}$ (**e–g**) components versus different polarization states of both $\boldsymbol{E}_1$ and $\boldsymbol{E}_1'$ ($G_1 = 22$ GHz and $G_1' = 20$ GHz). The solid dots are the measured results and the solid curves are the fitted theoretical ϕ values

P-polarized beams for choosing different transition pathways among various Zeeman sublevels as shown in Fig. 1(b), where $F_1 = (\Gamma_{10} + i\Delta_1) + (G_1^{\pm} + G_1'^{\pm})^2/\Gamma_{00} + (G_1^{\pm} + G_1'^{\pm})^2/\Gamma_{11}$ and $F_2 = \Gamma_{00} + (G_1^{\pm} + G_1'^{\pm})^2/(\Gamma_{10} + i\Delta_1) + (G_1^{\pm} + G_1'^{\pm})^2/(\Gamma_{01} - i\Delta_1)$ for the S-polarized beam pathways, and $F_1 = (\Gamma_{10} + i\Delta_1) + (G_1 + G_1')^2/\Gamma_{00} + (G_1 + G_1')^2/\Gamma_{11}$ and $F_2 = \Gamma_{00} + (G_1 + G_1')^2/(\Gamma_{10} + i\Delta_1) + (G_1 + G_1')^2/(\Gamma_{01} - i\Delta_1)$ for the P-polarized beam pathways, resulting in $n_2^{\mathrm{S}}(1.5\times10^{-8}\ \mathrm{cm}^2/W) > n_2^{\mathrm{P}}(1.2\times10^{-8}\ \mathrm{cm}^2/W)$ and $I_0^{\mathrm{S}} < I_0^{\mathrm{P}}$ for $|\rho_{10}^{\mathrm{S}}|^2 < |\rho_{10}^{\mathrm{P}}|^2$. So one can obtain $\phi^{\mathrm{S}} > \phi^{\mathrm{P}}$, where ϕ^{S} and ϕ^{P} are the nonlinear phase shifts of the $\boldsymbol{E}_{\mathrm{F}}^{\mathrm{S}}$ and $\boldsymbol{E}_{\mathrm{F}}^{\mathrm{P}}$ beams, respectively. From Fig. 3(e) the intensity of $\boldsymbol{E}_{\mathrm{F}}^{\mathrm{P}}$ is much stronger than that of $\boldsymbol{E}_{\mathrm{F}}^{\mathrm{S}}$ at $\theta = 0°$ and 90° due to $I_0^{\mathrm{S}} < I_0^{\mathrm{P}}$. Then, the y-direction splitting of the $\boldsymbol{E}_{\mathrm{F}}^{\mathrm{P}}$ beam is weaker than $\boldsymbol{E}_{\mathrm{F}}^{\mathrm{S}}$ due to $\phi^{\mathrm{S}} > \phi^{\mathrm{P}}$. Compared with $\boldsymbol{E}_{\mathrm{F}}^{\mathrm{S}}$ at $\theta = \pm 22.5°$ or 67.5°, the x-direction splitting of the $\boldsymbol{E}_{\mathrm{F}}^{\mathrm{P}}$ beam is too weak to be observed in Fig. 3(e).

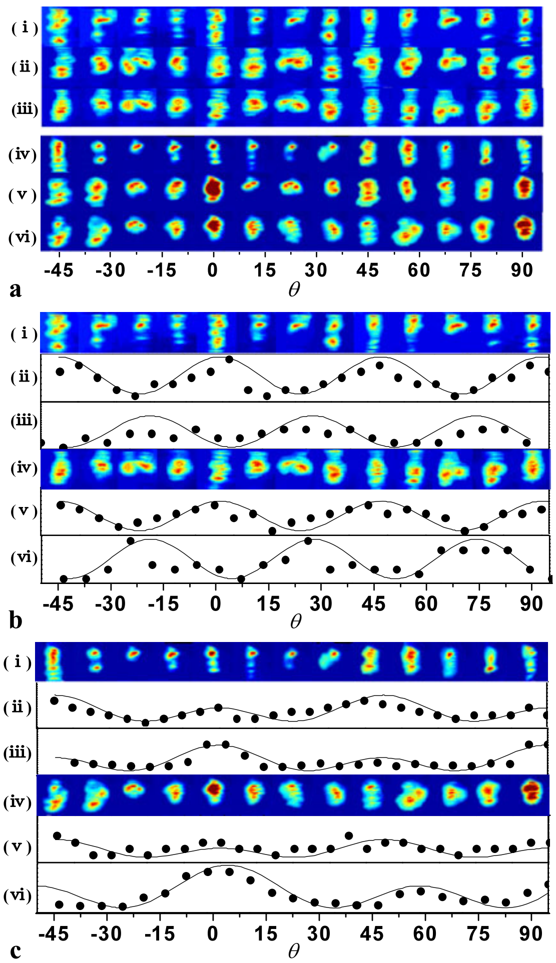

Fig. 4 (**a**) The measured beam spots of the E_F^S (*i–iii*) and E_F^P (*iv–vi*) fields with all five beams on (*i*, *iv*), without E_2 (*ii*, *v*), and without E_2 & E_2' (*iii*, *vi*) versus different polarization states of E_1&E_1'; (**b**) the measured beam spots and the beam splitting number of both the x (*iii*, *vi*), and y (*ii*, *v*) directions (*solid dots*) of the E_F^S beam with all five beams (*i–iii*), and without E_2 & E_2' (*iv–vi*); (**c**) the measured beam spots, the beam splitting number of the y (*ii*, *v*) direction (*solid dots*) and the intensity (*iii*, *vi*) of the E_F^P beam with all five beams (*i-iii*), and without E_2&E_2' (*iv–vi*). The solid curves are the fitted theoretical ϕ values ($G_1 = 22$ GHz, $G_1' = 20$ GHz, $G_2 = 2.0$ GHz and $G_2' = 1.8$ GHz)

When the E_2 and E_2' beams are turned on, Fig. 4 shows different dressing effects for the E_F^S and E_F^P components with changing E_1 & E_1' polarization states. Specifically, the splittings of both E_F^S and E_F^P beams have the same 45° period, as shown in Fig. 3. Comparing (i) with (iv) in Figs. 4(b) and 4(c), we can see that both E_F^S and E_F^P intensities in (i) are weaker due to the suppressions of E_2 and $E_2'(\Delta_1 + \Delta_2 = 0$ and $\Delta_1 = -10$ GHz), which causes a larger splitting in the y-direction ((ii) in Figs. 4(b) and 4(c)). For the E_F^S beam, at $\theta = \pm 22.5°$ or 67.5° without E_2 and E_2', it has the x-direction splitting ((iv) and (vi) in Fig. 4(b)). However, with five beams all on, E_F^S is shifted to the upper direction by E_2', and hardly overlaps with both E_1 and E_1' beams, causing the x-direction splitting to be weak ((i) and (iii) in Fig. 4(b)).

Moreover, in Figs. 4(b) and (c), the contrast ratio of the y-direction splitting $\eta = N_1/N_2$ turns to be $\eta = 0.29$ and $\eta = 0.65$ for $E_F^S(E_F^P)$ with or without E_2 and E_2' dressing, respectively. Here, N_1 and N_2 are the numbers of the y-direction splitting spots at valley and peak points of the curves (ii) in Figs. 4(b) and (c), respectively. We can observe that the contrast of periodic splitting in the y-direction becomes better with dressing fields E_2 and E_2' ((i) and (iv) in Figs. 4(b) and (c)). This behavior occurs because different polarization states of the pumping beams can select different transitions among Zeeman sublevels and have different dressing strengths [5].

4 Conclusion

We have experimentally observed spatial splitting of the dressed FWM beam when the polarizations of the pumping fields are changed. The periodically appearing spatial splitting is also investigated versus different polarization states and specially arranged spatial beam geometry in a ladder-type three-level system. The differences in periodic spatial splittings between the E_F^S and E_F^P components have also been studied. Theoretical simulations have been carried out based on the coupled propagation equations for the two polarization components of the generated FWM beam, which match quite well with the experimentally observed behaviors. Such studies can have potential applications in soliton deflection and splitting communication, spatial optical switch [14], and other quantum information processes.

Acknowledgements This work was supported by NSFC (10974151, 61078002, 61078020), NCET (08-0431), RFDP (20100201120031), 2009xjtujc08, XJJ20100100, XJJ20100151.

References

1. C.J. Zhu, A.A. Senin, Z.H. Lu, J.G. Eden, Phys. Rev. A **72**, 023811 (2005)
2. W.C. Magno, R.B. Prandini, P. Nussenzveig, S.S. Vianna, Phys. Rev. A **63**, 063406 (2001)
3. B. Wang, Y. Han, J. Xiao, X. Yang, C. Xie, H. Wang, M. Xiao, Opt. Lett. **31**, 3647 (2006)
4. H.Y. Ling, Y. Q Li, M. Xiao, Phys. Rev. A **53**, 1014 (1996)
5. A.M. Akulshin, S. Barreiro, A. Lezama, Phys. Rev. A **57**, 2996 (1998)
6. G.P. Agrawal, Phys. Rev. Lett. **64**, 2487 (1990)
7. R.S. Bennik, V. Wong, A.M. Marino, D.L. Aronstein, R.W. Boyd, C.R. Stroud Jr., S. Lukishova, Phys. Rev. Lett. **88**, 113901 (2002)
8. A.J. Stentz, M. Kauranen, J.J. Maki, G.P. Agrawal, R.W. Boyd, Opt. Lett. **17**, 19 (1992)
9. J. Miguel Hickmann, A.S.L. Gomes, Cid B. de Araújo, Phys. Rev. Lett. **68**, 3547 (1992)

10. H. Wang, D. Goorskey, M. Xiao, Phys. Rev. Lett. **87**, 073601 (2001)
11. W. Krolikowski, M. Saffman, B. Luther-Davies, C. Denz, Phys. Rev. Lett. **80**, 3240 (1998)
12. Y.P. Zhang, C.C. Zuo, H.B. Zheng, C.B. Li, Z.Q. Nie, J.P. Song, H. Chang, M. Xiao, Phys. Rev. A **80**, 055804 (2009)
13. Y.H. Xiao, M. Klein, M. Hohensee, L. Jiang, D.F. Phillips, M.D. Lukin, R.L. Walsworth, Phys. Rev. Lett. **101**, 043601 (2008)
14. A.M.C. Dawes, L. Illing, S.M. Clark, D.J. Gauthier, Science **308**, 672 (2005)